

Prussian Blue Analogues Derived Bimetallic CoNi@NC as Efficient Oxygen Reduction Reaction Catalyst for Mg-Air Batteries

Xiaoyang Dong,^[a, b] Jinxing Wang,^{*,[a, b]} Junqian Ling,^[a, b] Ying Zhang,^[a] Junyao Xu,^[a, b] Wen Zeng,^[a] Guangsheng Huang,^[a, b] Jingfeng Wang,^{*,[a, b]} and Fusheng Pan^[a, b]

The magnesium-air (Mg-air) batteries are regarded as a highly promising system for electrochemical energy conversion and storage, owing to their exceptional energy density, notable safety and eco-friendliness. The development of high-performance and durable non-noble metal catalysts for the cathodic oxygen reduction reaction (ORR) is crucial for advancing the practical use of Mg-air batteries. The synergistic interaction between different metals in bimetallic catalysts is an effective strategy for enhancing the activity and stability of the catalysts. Herein, various prussian blue analogues (PBA) were selected as precursors to synthesis the bimetallic CoNi@NC, monometallic Co@NC and Ni@NC catalysts due to tunable chemical composi-

tions. Compared with Co@NC and Ni@NC, the bimetallic CoNi@NC pyrolyzed at 600 °C (CoNi@NC-600) exhibits outstanding ORR performances and stability in alkaline (0.1 M KOH) and neutral (3.5 wt % NaCl) electrolytes. Following 5000 CV cycles, the half-wave potentials for CoNi@NC-600 show only minor negative shifts of 8 and 7 mV, respectively. Meanwhile, the CoNi@NC-600 possesses the similar ORR reaction mechanism and activity with Pt/C. The primary Mg-air battery assembled with CoNi@NC-600 displays better discharge performances than that of Co@NC and Ni@NC. This study lays the foundation for future investigations into the advancement of non-precious bimetallic catalysts for ORR in Mg-air batteries.

Introduction

The reliance on traditional fossil fuels, which contribute to global warming and environmental pollution, is no longer sustainable.^[1] There is an urgent need to develop electrochemical energy storage devices that offer high capacity, energy density, safety and cost-effectiveness.^[2,3] Metal-air batteries, particularly Mg-air batteries, are recognized as promising candidates for next-generation energy storage and conversion systems owing to their high crustal abundance, safety, energy density and environmental friendliness.^[4–6] Mg-air batteries stand out for their exceptional specific energy density, volumetric capacity, theoretical voltage, plentiful resources, low toxicity and operational safety.^[7–9] The primary Mg-air battery consists of three main components: Mg anode, electrolyte and air cathode. The cathode is designed to continuously uptake oxygen from the air as a reactant. The metal anode and the electrolyte can be easily replaced, enabling the battery to be “rechargeable”.^[10–12] Primary Mg-air batteries, typically utilizing an aqueous electrolyte, are considered promising power

sources for applications like emergency power supplies and backup energy systems.^[13] Unfortunately, the sluggish dynamics of ORR at cathode is a major obstacle for Mg-air batteries, significantly impeding their practical application.^[14–16] The advancement of high-efficiency catalysts that can enhance the kinetics of ORR is crucial for elevating the performances of batteries.^[17–19] While traditional noble-metal catalysts, such as Pt and Pd, are highly effective in catalyzing ORR, their scarcity, lack of durability and high costs present significant challenges to their widespread commercialization.^[20–22] Consequently, exploring high-performance and cost-effective non-noble metal catalysts for the ORR is both a critical necessity and formidable challenge in the advancement of Mg-air batteries.

Transition metal–nitrogen–carbon (M–N–C) materials, characterized by their M–N_x active centers, are adept at promoting the adsorption and dissociation of O₂ during the ORR, demonstrating superior intrinsic catalytic properties.^[16,23] The intrinsic characteristics and concentration of these M–N_x active sites are pivotal in dictating the ORR performance and stability of the materials.^[24] PBA represents a classic class of metal-organic frameworks (MOFs), which comprise transition metal ions and CN-containing ligands. The PBA possesses many merits such as straightforward synthesis, tunable chemical compositions, adjustable morphology and cost-effectiveness.^[25–28] Additionally, PBA is advantageous for the synthesis of M–N–C catalysts as it allows for a variety of metal atoms and nitrogen and carbon sources to be incorporated by adjusting the ligands of the anionic and cationic components, providing more versatility compared to other MOFs.^[29–31] In recent years, researchers have enhanced catalytic performance by incorporating a second metal into monometallic catalysts. This strategy

[a] X. Dong, J. Wang, J. Ling, Y. Zhang, J. Xu, W. Zeng, G. Huang, J. Wang, F. Pan
Chongqing University, School of Materials Science and Engineering,
Chongqing 400030, China
E-mail: wjx@cqu.edu.cn
jfwang@cqu.edu.cn

[b] X. Dong, J. Wang, J. Ling, J. Xu, G. Huang, J. Wang, F. Pan
Chongqing University, National Engineering Research Center for Magnesium Alloys, Chongqing 400030, China

 Supporting information for this article is available on the WWW under
<https://doi.org/10.1002/batt.202400418>

has effectively modified the active sites and optimized the reaction energy barriers with oxygen-containing intermediates in the ORR process, thereby boosting the catalytic performance of electrocatalysts.^[32,33] Yu et al successfully developed the bimetallic FeNi catalyst embedded in a nitrogen-doped carbon matrix. The incorporation of Ni atom modulates the electronic structure of the Fe atom, further reducing the activation energy for the rate-determining step in the ORR, improving the catalytic performances.^[34] Ahsan et al reported the synthesis of bimetallic NiCu alloy nanoparticles within a sp^2 carbon framework. The doping of Ni atom induces a lattice contraction and generates high strain energy that significantly enhances the ORR catalytic rate, which further accelerates the electron transfer rate at the active surface sites of the catalyst.^[35] Currently, the synthesis of bimetallic catalysts is complex and requires stringent conditions, with metal atoms tending to aggregate after pyrolysis, which hinders large-scale production and application. Utilizing PBA as precursors to explore efficient bimetallic catalysts and boost ORR performance is a promising strategy for advancing the cathode catalysts in Mg-air batteries.

Herein, the bimetallic CoNi@NC, monometallic Co@NC and Ni@NC were prepared by various PBA precursors under argon (Ar) atmosphere. The calcination temperature significantly influences the morphology and ORR performance of catalysts. The corresponding mechanisms of catalysts have been investigated in this study. Notably, the bimetallic CoNi@NC-600 demonstrates superior electrochemical performance and remarkable stability over the monometallic Co@NC and Ni@NC under both alkaline and neutral conditions. It also follows an ORR pathway akin to that of commercial Pt/C. Furthermore, the primary Mg-air battery consisted of CoNi@NC-600 shows enhanced discharge characteristics compared to one made with Co@NC and Ni@NC. This research presents a straightforward approach to the systematic exploration of bimetallic M–N–C catalysts and affirms the positive impact of metal atom synergy on enhancing ORR activity and stability.

Results and Discussion

Materials Characterization

The CoNi@NC-T catalysts were prepared by pyrolysis of CoNi-PBA precursor under Ar atmosphere. The pyrolysis temperature of the catalysts was determined by probing the thermal stability of the precursor. As illustrated in Figure 1a, the TGA curve of CoNi-PBA exhibits three distinct stages, corresponding to mass losses of 17.0%, 3.0% and 37.5%, respectively. The pyrolytic transformation of precursors into M@NC materials occurs in the third stage, which provides a basis for temperature selection for the preparation of catalysts. XRD analysis was used to characterize the crystal structure of CoNi-PBA and CoNi@NC-T catalysts. As displayed in Figure 1b, the diffraction characteristic peaks of CoNi-PBA match to typical layered Hofmann-type $Ni(H_2O)_2[Ni(CN)_4] \cdot xH_2O$ coordination polymer.^[36] The XRD diffraction patterns of the CoNi@NC-T ($T=500, 600$ and 700) catalysts are almost identical, indicating that they have similar crystal structures. The characteristic peaks at $44.2^\circ, 51.5^\circ$ and 75.9° in the CoNi@NC-T catalysts correspond to the (111), (200) and (220) crystal planes of metallic Co (PDF#15-0806), whereas the peaks at $44.5^\circ, 51.8^\circ$ and 76.3° match to the (111), (200) and (220) crystal planes of metallic Ni (PDF#04-0850).^[37] The diffraction patterns of CoNi@NC-T catalysts all show broader peaks near 26.4° , which attributed to the (002) plane of graphite C (PDF#41-1487).^[38] The structural defects of the CoNi@NC-T catalysts were characterized with Raman spectroscopy and the results were shown in Figure 1c. The Raman spectra of CoNi@NC-T exhibit two characteristic peaks of carbon materials at 1342 and 1580 cm^{-1} , corresponding to the D and G. The intensity ratio (I_D/I_G) between the D peak and the G peak is utilized to quantitatively assess the defect and graphitization degree of carbon materials.^[39] The I_D/I_G ratios for the CoNi@NC-500, CoNi@NC-600 and CoNi@NC-700 catalysts are 1.17 , 1.14 , and 0.88 . Choosing the suitable pyrolysis temperature to balance the degree of defects and graphitization can improve

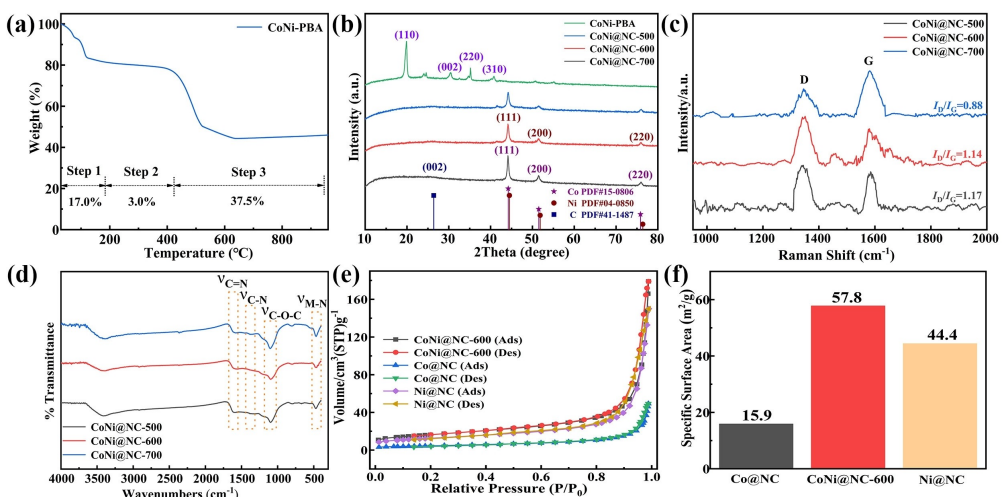


Figure 1. (a) TGA curve of CoNi-PBA precursor. (b) The XRD patterns of CoNi-PBA precursor and CoNi@NC-T ($T=500, 600$ and 700) catalysts. (c) Raman spectra. (d) FT-IR spectra. (e) N_2 adsorption/desorption plots. (f) Corresponding specific surface areas.

the ORR performances of catalyst. Figure 1d presents the FT-IR spectra of CoFe@NC-T catalysts. The spectral characteristics of the three are highly consistent, with the positions of the characteristic absorption peaks being nearly identical, indicating that they possess similar chemical bonds and functional group compositions. The M–N bond, evident within the wavenumber range of 450–500 cm⁻¹, signifies the coordination configuration established between transition metals M (M=Fe and Co) and nitrogen (N) atoms. The occurrence of C–N bond absorption peaks in the wavenumber range of 1250–1480 cm⁻¹ and C=N bond absorption peaks in the wavenumber range of 1510–1700 cm⁻¹ are indicative of the N-atom doped carbon material in the catalysts as well as the coexistence state of N and C elements.^[40] As depicted in Figure 1e, the N₂ adsorption-desorption curves for both the bimetallic CoNi@NC-600 and the monometallic Co@NC and Ni@NC catalysts all display pronounced hysteresis loops, which are characteristic of the typical IV isotherm. This suggests that all three catalysts possess mesoporous structures. As revealed in Figure 1f, the specific surface areas of Co@NC, CoNi@NC-600 and Ni@NC are 15.9, 57.8 and 44.4 m² g⁻¹, respectively. The synergistic interactions among the different metals contribute to a significant enhancement in the catalyst's specific surface area. The bimetallic CoNi@NC-600 catalyst, with its high specific surface area and mesoporous structure, significantly enhances the

exposure density of active sites for both Co and Ni. It also improves the accessibility of oxygen and electrolyte to the three-phase interface. Consequently, the bimetallic CoNi@NC-600 catalyst is likely to exhibit superior catalytic activity of ORR.

To investigate the surface elemental composition and chemical valence states of different catalysts, XPS was utilized for the characterization and analysis. The XPS spectra of Co@NC catalyst are displayed in Figure 2a-d. As presented in Figure 2a, there are Co, N, C, and O elements existing on the surface of the Co@NC. It can be seen from Figure 2b that the high-resolution spectrum of Co 2p_{3/2} has been divided into four types of peaks. The characteristic peaks located at binding energies of 778.3, 780.0, 781.6 and 783.9 eV are corresponded to Co⁰, Co²⁺, Co³⁺ and satellite peak, respectively.^[41] As revealed in Figure 2c, the peaks at 398.4, 399.1, 400.5 and 402.1 eV in the high-resolution spectrum of N 1s match to Pyridinic-N, Co–N, Pyrrolic-N and Graphitic-N. As shown in Figure 2d, the peaks at 284.7, 285.5, 286.5 and 288.4 eV represent the C–C, C–N, C=N, and O=C–O. Figure 2e presents the XPS survey spectrum of the Ni@NC catalyst, indicating the presence of Ni, N, C and O elements on the catalyst surface. The peaks at 852.6, 854.2, 856.0, 859.9 eV of Ni 2p_{3/2} are assigned to Ni⁰, Ni²⁺, Ni³⁺ valence states and satellite peak in the Figure 2f.^[42] As displayed in Figure 2g, the N 1s high-resolution spectrum of Ni@NC exists Pyridinic-N, Ni–N, Pyrrolic-N and Graphitic-N. The C 1s high-

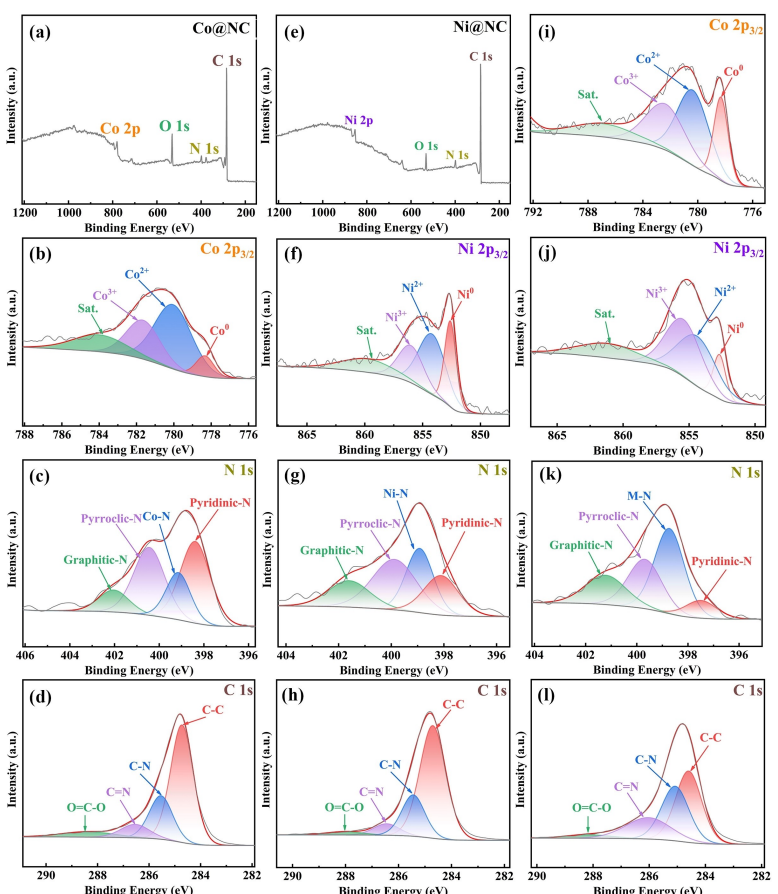


Figure 2. (a-d) The full XPS spectrum of Co@NC, high resolution XPS spectra of Co, N and C elements. (e-h) The full XPS spectrum of Ni@NC, high resolution XPS spectra of Ni, N and C elements. (i-l) High resolution XPS spectra of Co, Ni, N and C elements in the CoNi@NC-600.

resolution spectrum possesses C–C, C–N, C=N and O=C–O species in Figure 2h. The elemental high-resolution spectra of CoNi@NC-600 are shown in Figure 2i–l. The high-resolution spectrum of Co 2p_{3/2} has been split in four forms in Figure 2i that Co⁰, Co²⁺, Co³⁺ and satellite peak locating at 778.3, 780.4, 782.4 and 786.9 eV. As revealed in Figure 2j, the peaks at 852.7, 854.4, 855.4 and 861.2 eV in the high-resolution spectrum of Ni 2p_{3/2} represent Ni⁰, Ni²⁺, Ni³⁺ valence states and satellite peak. As shown in Figure 2k, the high-resolution XPS spectrum of N 1s exists in four configurations: Pyridinic-N, M–N (M=Co/Ni), Pyrrolic-N and Graphitic-N. Figure 2l presents the high-resolution XPS spectrum of the C 1s, demonstrating the presence of C–C, C–N, C=N, and O=C–O bond groups. The XPS survey spectrum and high-resolution spectra of individual elements for CoNi@NC-T (T=500, 600 and 700) catalysts are shown in Figure S1. The XPS survey spectra of CoNi@NC-T indicate the presence of elements Co, Ni, N, C and O on the surface of the catalyst. The presence of Co⁰ and Ni⁰ suggests the CoNi@NC-T surface contain metallic Co and Ni, and it also signifies that Ni has been successfully incorporated.^[43,44] The presence of O 1s is attributed to the oxidation when the catalyst is exposed to air. The above results demonstrate the bimetallic CoNi@NC-T catalysts have been successfully prepared.

To investigate the micromorphology and structure of as-prepared precursors and electrocatalysts, the SEM, EDS and TEM techniques were utilized for analysis. Figure 3a–f exhibit the SEM images and corresponding EDS mapping of the constituent elements for the bimetallic CoNi@NC-T (T=500, 600 and 700) catalysts. In the EDS mapping of the CoNi@NC-T catalysts, the presence of Co, Ni, N and C elements is observed and uniformly distributed across the surface of catalysts. The SEM images and elemental EDS mappings of monometallic Co@NC and Ni@NC catalysts are depicted in Figure S2. Both

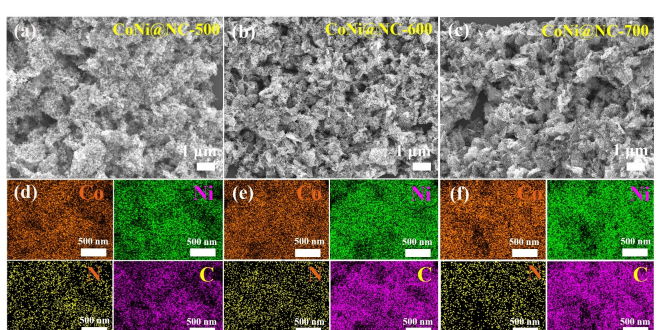


Figure 3. (a–c) SEM images of CoNi@NC-T (T=500, 600 and 700) catalysts. (d–f) EDS mapping images of CoNi@NC-T.

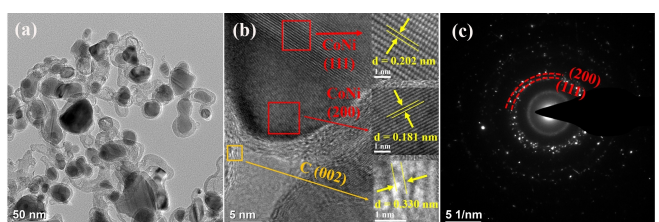


Figure 4. CoNi@NC-600 (a) TEM image. (b) HRTEM image. (c) SAED.

monometallic catalysts exhibit the presence of N and C elements, but each contains only one type of metal element (Co or Ni). The EDS mapping results between bimetallic and monometallic catalysts further substantiates the successful incorporation of the second metal Ni.

Figure 4a is the TEM image of CoNi@NC-600, confirming that the catalyst has a core-shell structure. Figure 4b presents the HRTEM image of CoNi@NC-600, from which the diffraction fringes of the catalyst particles can be clearly observed. The lattice spacing of 0.202 and 0.181 nm within the red square correspond to the (111) and (200) planes of metallic CoNi, while the lattice spacing of 0.330 nm within the yellow square corresponds to the (002) plane of graphite carbon. Figure 4c displays the SAED of the CoNi@NC-600 catalyst, where the diffraction rings correspond to the (111) and (200) planes of metallic CoNi.^[38] The above results are consistent with the findings from XRD and XPS, confirming the successful synthesis of the bimetallic CoNi@NC catalyst.

The Electrochemical Data of ORR

The intrinsic ORR catalytic activities and stability of as-synthesized CoNi@NC-T (T=500, 600 and 700) and commercial Pt/C catalysts were evaluated with a rotating disk electrode in different electrolytes. First, the cyclic voltammetry (CV) tests of the bimetallic CoNi@NC-T catalysts were performed in a 0.1 M KOH solution saturated with N₂ and O₂ to evaluate the ORR activities of catalysts. Figure 5a and 5b present the CV curves of CoNi@NC-T catalysts in N₂-saturated and O₂-saturated KOH solutions, respectively. The observation that the CV curves exhibit obvious reduction peaks for the ORR only under O₂-saturated conditions indicates that the ORR process requires the participation of O₂. The reduction peak potentials for the CoNi@NC-T (T=500, 600 and 700) catalysts are 0.821, 0.837 and 0.804 V, respectively. Notably, the CoNi@NC-600 demonstrates a more positive reduction peak potential, signifying its superior catalytic activity towards the ORR. In order to further investigate the ORR activities of catalysts, the linear sweep voltammetry (LSV) tests were also conducted with O₂-saturated KOH solution under various rotating rates. Figure 5c–e present the LSV curves of the bimetallic CoNi@NC-T (T=500, 600 and 700) catalytic materials at rotation speeds ranging from 400 to 2000 rpm. As the rotation speed increases, the limiting diffusion current density of CoNi@NC-T shows an upward trend, which is attributed to the enhanced diffusion rate of O₂ because of the increased rotation speed.^[45] Figure S3a–c display the Koutecky-Levich (K–L) plots derived from the LSV curves of CoNi@NC-T at various rotation speeds. The K–L plots exhibit a good linear relationship and even overlap at different potentials, indicating that the ORR process occurring on the bimetallic CoNi@NC catalysts conform to the characteristics of a first-order reaction kinetics.^[46] Figure 5f exhibits the LSV curves of CoNi@NC-T catalysts at 1600 rpm. The CoNi@NC-600 displays more high onset potential, half-wave potential and large limiting diffusion current density (0.90 V, 0.82 V, 4.75 mA cm⁻²) than that of CoNi@NC-500 (0.89 V, 0.81 V, 4.52 mA cm⁻²) and CoNi@NC-700

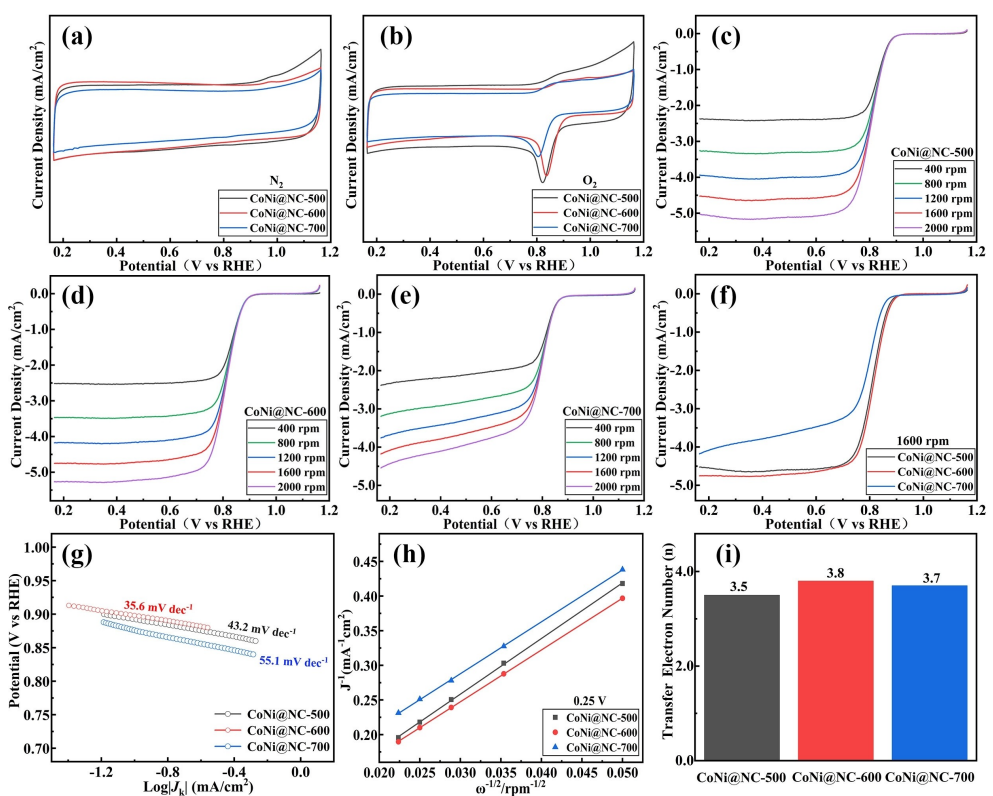


Figure 5. CoNi@NC-T ($T = 500, 600$ and 700) catalysts (a, b) CV curves under N_2 -saturated and O_2 -saturated electrolytes. (c–e) LSV curves at different rotating rates. (f) LSV curves of 1600 rpm. (g) Tafel slope. (h) K–L plots at 0.25 V. (i) Transfer electron number.

(0.88 V, 0.79 V, 4.18 mA cm^{-2}). As shown in Figure 5g, the Tafel slopes of the CoNi@NC-T ($T = 500, 600$ and 700) catalysts are 43.2 , 35.6 and 55.1 mV dec^{-1} , respectively. The CoNi@NC-600 processes the smallest slope, indicating that it has the fastest ORR kinetics. Figure 5h displays the K–L plots of CoNi@NC-T ($T = 500, 600$ and 700) catalysts at 0.25 V, indicating that all catalysts conform to the characteristics of a first-order kinetic reaction with respect to O_2 . The CoNi@NC-600 has the smallest slope, reflecting its excellent intrinsic reaction rate for the ORR. As depicted in Figure 5i, the electron transfer number (n) at 0.25 V for the catalysts can be calculated from the slopes of the K–L plots. The n of CoNi@NC-T ($T = 500, 600$ and 700) catalysts are 3.5 , 3.8 and 3.7 , respectively. The value of n for CoNi@NC-600 is closer to the theoretical value of 4 , indicating a higher selectivity for the $4 e^-$ pathway of ORR.

To investigate the impact of synergistic effects between different metals on the ORR performances, a comparative study was conducted between the monometallic Co@NC and Ni@NC, bimetallic CoNi@NC-600 and commercial Pt/C catalysts. Figure 6a illustrates the CV curves of various catalysts in an O_2 -saturated alkaline electrolyte. The oxygen reduction peak potentials for the Co@NC and Ni@NC, CoNi@NC-600 and Pt/C catalysts are 0.807 , 0.705 , 0.836 and 0.861 V, respectively. Compared to Co@NC and Ni@NC, the CoNi@NC-600 catalyst exhibits a higher reduction peak potential, with only a 25 mV difference from Pt/C, demonstrating its superior catalytic activity for the ORR. Figure S3d–f display the LSV curves of the Co@NC, Ni@NC and Pt/C catalysts at various rotation speeds.

The continuous increase in limiting diffusion current density with the increase in rotation speed indicates that the ORR process for all catalysts is governed by kinetic reactions. Figure 6b presents the LSV curves of all catalysts at 1600 rpm. The bimetallic CoNi@NC-600 catalyst demonstrates exceptional performance, with an onset potential, half-wave potential, and limiting diffusion current density recorded at 0.90 V, 0.82 V, and 4.75 mA cm^{-2} , respectively. These values are notably more advantageous than those observed for the monometallic Co@NC catalyst (0.88 V, 0.80 V, 4.02 mA cm^{-2}) and the Ni@NC catalyst (0.85 V, 0.70 V, 4.01 mA cm^{-2}). The Tafel slopes of catalysts are depicted in Figure 6c. The slopes for the Co@NC, Ni@NC, CoNi@NC-600 and Pt/C catalysts are 54.0 , 91.6 , 40.7 and 86.3 mV dec^{-1} , respectively. The CoNi@NC-600 catalyst has the smallest slope, indicating that it possesses the lowest intrinsic reaction over-potential and the fastest kinetic rate in the ORR process. Figure 6d displays the K–L plots of the various catalysts at 0.25 V. The K–L plots for the CoNi@NC-600 and Pt/C catalysts exhibit good linear fits with similar slopes, indicating that they share comparable kinetic characteristics in the ORR. As shown in Figure 6e, the electron transfer number (n) for the Co@NC, Ni@NC, CoNi@NC-600 and Pt/C catalysts are 3.9 , 3.4 , 3.8 and 3.9 , severally. The value of n for the CoNi@NC-600 is close to that of the Pt/C. Additionally, the stability of the catalyst is one of the crucial metrics for assessing ORR performance. Accelerated aging tests were conducted on the all catalysts, with the shift in the half-wave potential before and after 5000 cycles of CV as the criterion for evaluating stability. Figure 6f–i show the LSV

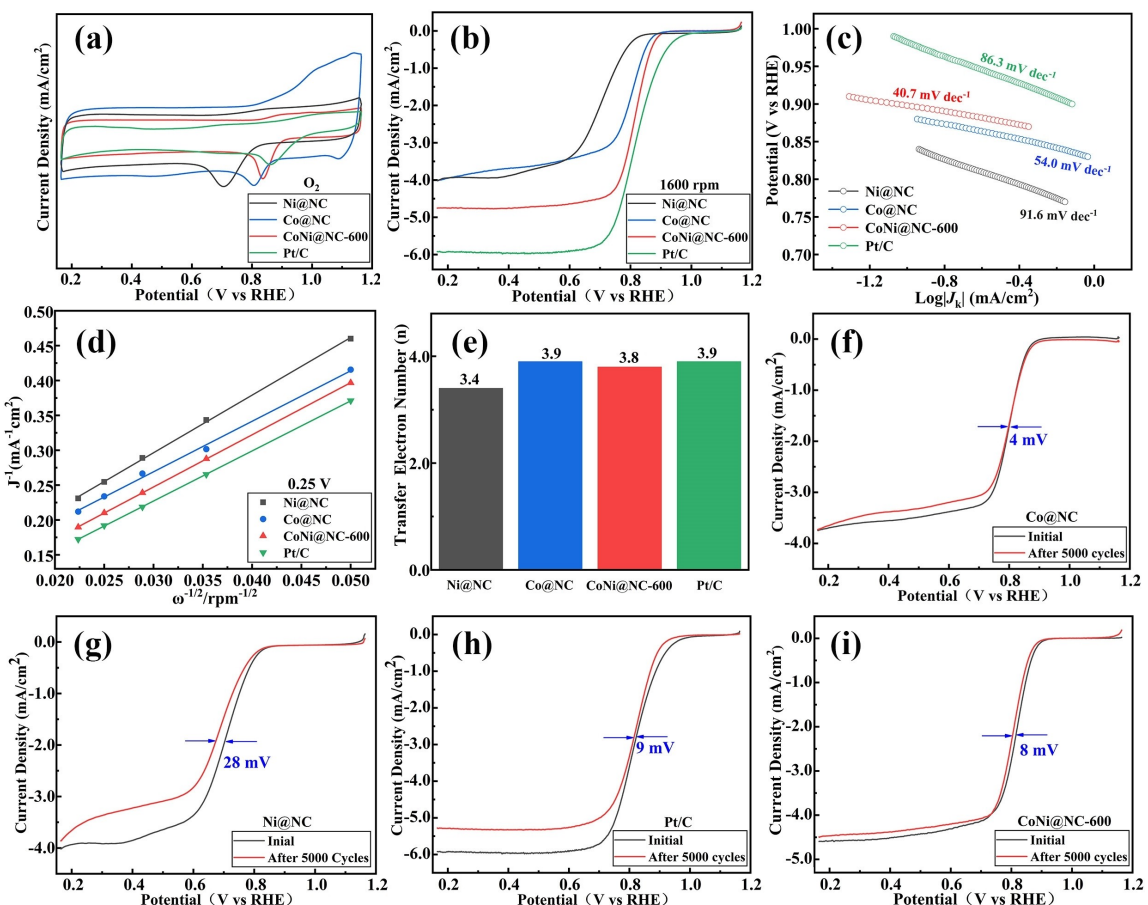


Figure 6. The ORR performances of different catalysts (a) CV curves. (b) LSV curves of 1600 rpm. (c) Tafel slope. (d) K–L plots at 0.25 V. (e) Transfer electron number. (f–i) LSV curves before and after 5000 CV cycles of Co@NC, Ni@NC, Pt/C and CoNi@NC-600.

curves of the Co@NC and Ni@NC, Pt/C, and CoNi@NC-600 catalysts before and after 5000 CV cycles in a 0.1 M KOH alkaline solution, with negative shifts in the half-wave potential of 4, 28, 9 and 8 mV, respectively. The bimetallic CoNi@NC-600 demonstrates superior stability compared to the commercial Pt/C, although it is not as stable as the monometallic Co@NC. However, under the synergistic effect of the bimetallic combination, there is a significant enhancement in current density of Co@NC, and the stability of the Ni@NC is notably improved. In summary, the ORR performance of the bimetallic CoNi@NC-600 is significantly superior to that of the monometallic Co@NC and Ni@NC catalysts. This enhancement is attributed to the presence of Co, which elevates the oxygen reduction peak potential of the catalyst, and the doping of Ni, which enhances the limiting diffusion current density. The synergistic interaction between Co and Ni collectively enhances electrochemical performances of catalyst for the ORR.^[38,43]

To further explore the potential application of the bimetallic CoNi@NC as cathode catalysts for Mg-air batteries, the electrochemical performances of as-prepared catalysts were tested in a 3.5 wt% NaCl neutral electrolyte. Figure 7a illustrates the CV curves of the CoNi@NC-T ($T=500, 600$ and 700) catalysts, all of which exhibit distinct reduction peaks. The oxygen reduction peak potentials are 0.523, 0.530 and 0.531 V, severally. Fig-

ure S4a–c display the LSV curves of CoNi@NC-T catalysts in NaCl electrolyte at rotation speeds ranging from 400 to 2000 rpm. The LSV curves of all catalysts exhibit phenomena similar to those observed in alkaline electrolyte: as the rotation speed increases, the limiting diffusion current density also continuously increases. This indicates that the ORR process on the catalysts in neutral electrolyte is also controlled by kinetic reactions. The LSV curves of CoNi@NC-T catalysts at 1600 rpm are depicted in Figure 7b. The CoNi@NC-600 demonstrates the highest onset potential (0.66 V) and the largest limiting diffusion current density (5.51 mA cm^{-2}), surpassing those of CoNi@NC-500 (0.65 V, 4.26 mA cm^{-2}) and CoNi@NC-700 (0.64 V, 3.54 mA cm^{-2}). Regarding the half-wave potential, the CoNi@NC-600 is only 10 mV lower than that of CoNi@NC-500. As shown in Figure 7c, the Tafel slopes of the bimetallic CoNi@NC-T ($T=500, 600$ and 700) catalysts are 80.7, 73.1, and 80.4 mV dec^{-1} , respectively. The CoNi@NC-600 exhibits the smallest Tafel slope, which substantiates its fastest kinetic rate for ORR. Figure S4d–f present the K–L plots for the CoNi@NC-T ($T=500, 600$ and 700) catalysts within the potential range of 0.05 to 0.20 V. The K–L plots at various potentials all exhibit a good linear relationship, and even overlap, indicating that the catalysts still conform to the characteristics of first-order kinetic reactions in the neutral electrolyte. Figure 7d displays the K–L

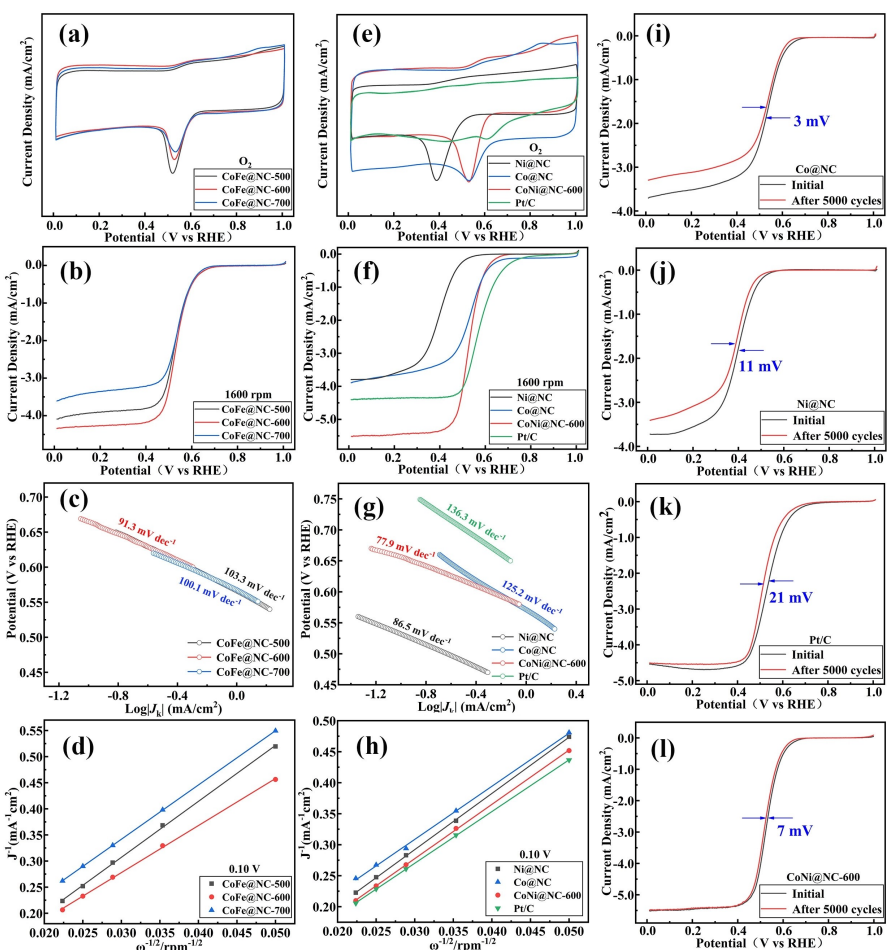


Figure 7. CoNi@NC-T ($T = 500, 600$ and 700) catalysts (a) CV curves. (b) LSV curves of 1600 rpm. (c) Tafel slope. (d) K–L plots at 0.10 V. The ORR performances of different catalysts (e) CV curves. (f) LSV curves of 1600 rpm. (g) Tafel slope. (h) K–L plots at 0.10 V. (i–l) LSV curves before and after 5000 CV cycles.

plots of the CoNi@NC-T catalysts at 0.10 V. The CoNi@NC-600 has the lowest slope in the K–L plot, reflecting its fastest kinetic reaction. Figure 7e shows the CV curves of the all catalysts under O_2 -saturated condition, indicating the catalysts exhibit excellent ORR activity. Among them, the bimetallic CoNi@NC-600 has an oxygen reduction peak potential of 0.530 V, which is higher than that of the monometallic Co@NC and Ni@NC and is only 76 mV lower than that of Pt/C. This suggests that the synergistic effect between the bimetallic components can enhance the ORR activity. As shown in Figure S5a and S5b, CV curves for all catalysts under N_2 -saturated condition were also examined, revealing no distinct peaks. Figure S5c–e represent the LSV curves of the Co@NC, Ni@NC and Pt/C catalysts at various rotation speeds. The limiting diffusion current density continuously increases with the enhancement of rotation speed, indicating that the ORR process is controlled by kinetic reactions. Figure 7f presents the LSV curves of various catalysts at 1600 rpm. Compared to the monometallic catalysts, the ORR performance of the bimetallic CoNi@NC-600 is enhanced, indicating that the synergistic effect between different metals effectively improves the catalytic activity for ORR. Furthermore, the limiting diffusion current density of CoNi@NC-600 reaches up to 5.51 mAcm⁻², which is superior to that of the Pt/C,

suggesting that it possesses the fastest kinetic response. Figure 7g illustrates the Tafel slopes of the various catalysts in the low over-potential region. The Tafel slopes for the Co@NC, Ni@NC, CoNi@NC-600 and Pt/C are 125.2 , 86.5 , 77.9 and 136.3 mVdec⁻¹, respectively. Among them, the CoNi@NC-600 has the smallest slope, indicating the highest kinetic reaction rate. Figure 7h presents the K–L plots of the different catalysts at 0.10 V. The slopes of the K–L plots for the CoNi@NC-600 and Pt/C are the closest to each other, indicating that they have similar ORR processes and comparable catalytic activities. The stability of the monometallic Co@NC, Ni@NC, bimetallic CoNi@NC-600 and Pt/C catalysts in NaCl solution was also evaluated, with the outcomes shown in Figure 7i–l. After 5000 cycles, the half-wave potentials of the catalysts experienced negative shifts of 3 , 11 , 7 and 21 mV, respectively. Compared to Ni@NC, the doping of Co in the bimetallic catalyst effectively enhances the stability of Ni@NC. The incorporation of Ni significantly elevates the limiting diffusion current density of catalyst, surpassing the performance of Co@NC. Therefore, the synergistic effect between the two metals not only effectively promotes the ORR activity of catalyst but also improves its stability and limiting diffusion current density.

The Performances of Mg-air Batteries

Due to the excellent ORR activities and stability of synthesized materials in neutral electrolyte, the primary Mg-air batteries with monometallic and bimetallic materials as cathode catalysts were made to explore the feasibility in practical application. Figure 8a represents the open-circuit voltage (OCV) of Mg-air batteries. The Mg-air battery based on CoNi@NC-600 exhibits the highest average OCV of approximately 1.70 V, which is superior to those based on Co@NC and Ni@NC. The OCVs of both the CoNi@NC-600-based and Co@NC-based batteries are stable, while the Ni@NC-based battery shows significant fluctuations, which may be related to the stability of catalyst. Figure 8b displays the discharge curves of the Mg-air batteries at a current density of 1 mA cm^{-2} . After nearly 50 h of discharge, the CoNi@NC-600-based battery maintains an average voltage of approximately 1.40 V with a stable discharge plateau. In comparison, the Co@NC-based battery exhibits a slightly lower average voltage of about 1.37 V. The Ni@NC-based battery, however, shows a sloping discharge profile, indicating an unstable discharge process, which correlates with the observed stability in the OCV. The discharge performance at a higher current density of 5 mA cm^{-2} is shown in Figure 8c. Both the CoNi@NC-600-based and Co@NC-based batteries sustain stable discharge plateaus with average voltages of approximately 1.25 and 1.23 V, respectively. The Ni@NC-based battery has a lower

average voltage, around 1.14 V. Figure 8d illustrates the discharge curves at an even higher current density of 10 mA cm^{-2} . The CoNi@NC-600-based battery demonstrates the most stable platform with the highest average voltage, which is about 1.12 V. The average voltages for the Co@NC and Ni@NC-based batteries are 1.10 and 0.99 V, respectively. Figure 8e illustrates the rate performance of Mg-air batteries. Within the range of 10 to 50 mA cm^{-2} , the CoNi@NC-600-based battery demonstrates the most stable discharge platform and the highest discharge voltage, highlighting its stability at high current densities. However, when the current density reaches 50 mA cm^{-2} , the discharge voltage becomes too low, making it difficult to distinguish the impact of different catalysts on the battery performance. Figure 8f presents the polarization and power density curves of Mg-air batteries. The polarization curve of the CoNi@NC-600-based battery exhibits a broader current density range compared to the monometal-based batteries, with a stable curve. The maximum power density of the bimetallic Mg-air battery is 19.6 mW cm^{-2} , which is higher than that of Co@NC-based (19.1 mW cm^{-2}) and Ni@NC-based (16.7 mW cm^{-2}) batteries. At the same current density, the CoNi@NC-600-based battery achieves the highest power density. Furthermore, the Mg-air battery assembled with the bimetallic CoNi@NC-600 catalyst demonstrates the optimal discharge performance, aligning with its outstanding catalytic activity for the ORR in neutral electrolyte solution.

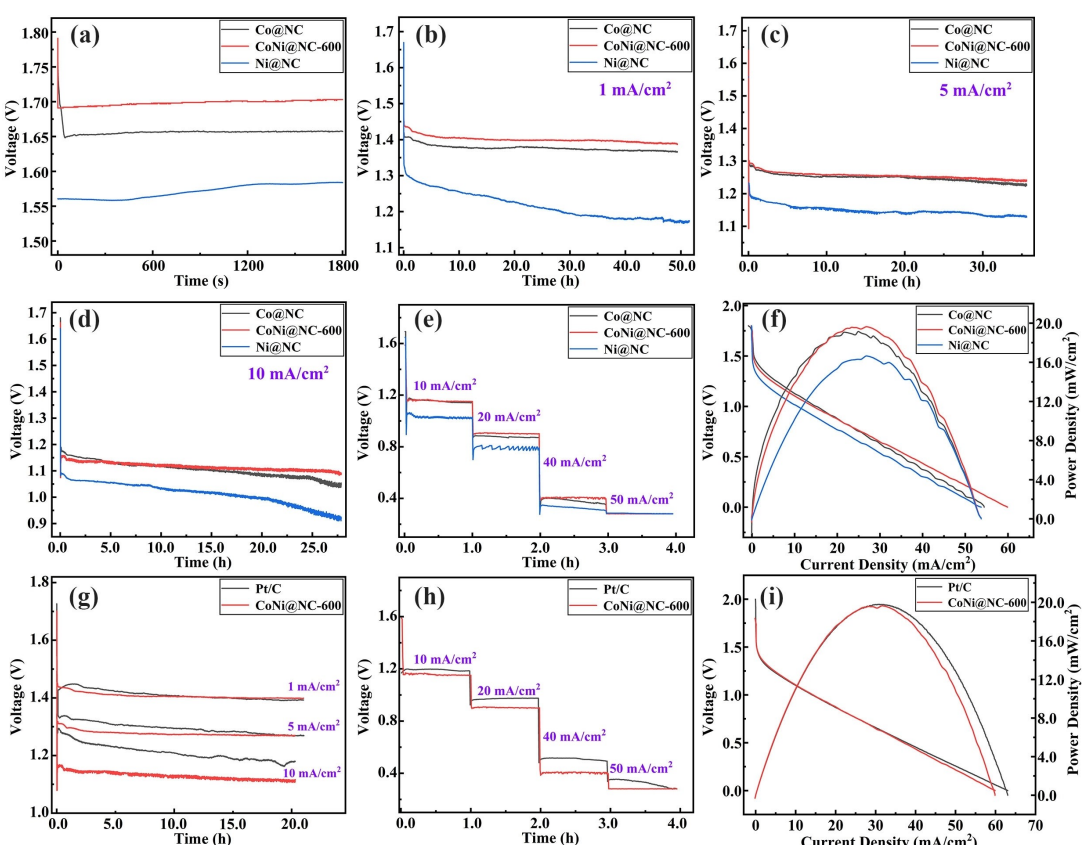


Figure 8. Performances of Mg-air batteries assembled with Co@NC, CoNi@NC-600 and Ni@NC catalysts (a) Open circuit voltage. (b-d) Discharge curves at 1, 5 and 10 mA cm^{-2} . (e) Rate performance. (f) Polarization curves and power density curves. Performances of Mg-air batteries assembled with CoNi@NC-600 and Pt/C catalysts: (g) Discharge curves at different current densities. (h) Rate performance. (i) Polarization curves and power density curves.

To validate the application potential of CoNi@NC-600, it was assembled into Mg-air battery separately from commercial Pt/C catalysts for a comparative discharge performances evaluation. Figure 8g shows the discharge curves of Mg-air batteries assembled with these two catalysts at different current densities. At the current density of 1 mA cm^{-2} , the bimetallic-based battery achieves an average discharge voltage of 1.42 V, which is slightly higher than that of the Pt/C-based battery at 1.41 V, accompanied by a more stable discharge platform. When the current density is increased to 5 mA cm^{-2} , the Pt/C-based battery shows a higher average discharge voltage compared to the CoNi@NC-600-based battery, with the bimetallic-based battery maintaining a steady platform. At 10 mA cm^{-2} , the Pt/C-based battery demonstrates slightly superior discharge performance. Nevertheless, the average voltages are nearly identical for both, with 1.20 V for the Pt/C and 1.13 V for the CoNi@NC-600, with the CoNi@NC-600-based battery sustaining a stable discharge platform. As the current density increases, the discharge platform of the Mg-air batteries lowers, and the average discharge voltage decreases. Additionally, rate capability tests were conducted with the results shown in Figure 8h. At current densities ranging from 10 to 50 mA cm^{-2} , the average voltage of the Pt/C-based battery is higher than that of the CoNi@NC-600-based battery. However, at 50 mA cm^{-2} , the discharge platform of the Pt/C-based battery drops significantly, with a decrease in stability. In contrast, the bimetallic CoNi@NC-600-based battery exhibits a more stable discharge platform within this range, suitable for high current density discharge, demonstrating excellent stability. Figure 8i presents the polarization and power density curves for Mg-air batteries based on both the bimetallic CoNi@NC-600 and Pt/C catalysts. The polarization curves indicate that the two are nearly coincident in the initial phase, but the Pt/C-based battery has a broader range of current densities. The Pt/C-based battery has a higher power density at the same current density, making it suitable for high current density discharge. The maximum power density of the CoNi@NC-600-based battery is 19.6 mW cm^{-2} , which is only 0.2 mW cm^{-2} less than that of Pt/C, demonstrating its excellent battery performance. Therefore, the bimetallic CoNi@NC-600 shows great potential as a cathode catalyst for Mg-air batteries.

Conclusions

In summary, the CoNi-PBA was prepared with a facile co-precipitation method and further used as the precursor to synthesize the bimetallic CoNi@NC catalysts. Compared with the monometallic Co@NC and Ni@NC catalysts, the CoNi@NC-600 exhibits superior ORR activities and stability in alkaline (0.1 M KOH) and neutral (3.5 wt % NaCl) solutions. In alkaline solution, the half-wave potential of CoNi@NC-600 is close to 0.82 V, differing from the commercial Pt/C by only 10 mV. The electron transfer number for its ORR is 3.8, which is close to the 3.9 of Pt/C, indicating that both have a similar ORR mechanism. In neutral solution, the limiting diffusion current density of CoNi@NC-600 is 5.51 mA cm^{-2} , which is significantly higher than

that of Pt/C (4.40 mA cm^{-2}). This can be attributed to its characteristic of having a larger specific surface area. The Tafel slope of CoNi@NC-600 is 77.9 mV dec^{-1} , which is better than that of Pt/C ($136.3 \text{ mV dec}^{-1}$), indicating its excellent catalytic performance for ORR. After 5000 CV cycles, the half-wave potential of CoNi@NC-600 displays only a negative shift of 8 mV in alkaline electrolyte and 7 mV in neutral electrolyte, demonstrating significantly better stability compared to Pt/C. The primary Mg-air battery was also assembled with the as-prepared catalysts and measured at the same situation. The Mg-air battery based on the CoNi@NC-600 catalyst exhibits superior discharge performance compared to batteries based on Co@NC and Ni@NC catalysts. This improvement can be attributed to the excellent ORR activity and stability of CoNi@NC-600. The synergistic effect of bimetallic metals can effectively enhance ORR performances of catalysts and promote the discharge performances of Mg-air batteries. This work lays the groundwork for future research into the development of bimetallic ORR catalysts for Mg-air batteries.

Experimental Section

Synthesis of Various PBA Precursors

The information on the chemical reagents used in this work can be found in the Supporting Information. The PBA precursors were synthesized by a simple co-precipitation at room temperature. The preparation of the CoNi-PBA precursor was conducted as follows: 6 mmol $\text{CoSO}_4 \cdot 7\text{H}_2\text{O}$ and 9 mmol $\text{K}_3\text{C}_6\text{H}_5\text{O}_7 \cdot \text{H}_2\text{O}$ were placed into a beaker containing 75 mL H_2O and 25 mL ethanol. After magnetic stirring for 30 min, a pink clear solution was obtained and designated as solution A. 4 mmol $\text{K}_2\text{Ni}(\text{CN})_4$ and 8 mmol $\text{C}_2\text{H}_4\text{N}_4$ were dissolved in 100 mL H_2O , stirring for 30 min, and designated as solution B. While continuously stirring solution A, slowly add solution B dropwise. After the completion of the addition, 10 mL $\text{NH}_3 \cdot \text{H}_2\text{O}$ was immediately introduced into the mixture. The resulting solution was stirred for 30 min and then aged at room temperature for 24 h. The final mixture was subjected to alternate centrifugal washing with water and ethanol several times until the supernatant was clear. The precipitate obtained from centrifugation was placed in a vacuum drying oven and dried at 80°C for 12 h to yield a brown product, named as CoNi-PBA. The preparation process for Co-PBA and Ni-PBA precursors can be referenced in the Supporting Information.

Preparation of CoNi@NC-T, Co@NC and Ni@NC Catalysts

The CoNi@NC-T catalysts were prepared by calcining the CoNi-PBA precursor in a tubular furnace under Ar atmosphere. The pyrolysis procedure was as follows: the temperature was ramped up at a rate of 2°C min^{-1} from room temperature to 350°C , where it was held for 1 h. The temperature was then further increased to the target temperature ($T = 500, 600$ and 700°C) and held for 2 h, after which the furnace was allowed to cool naturally to room temperature. The final products were the CoNi@NC-T catalysts. Based on the target temperature, the catalysts were named CoNi@NC-500, CoNi@NC-600 and CoNi@NC-700, respectively. The Co@NC catalyst was obtained by pyrolyzing the Co-PBA precursor at 600°C , following the same temperature program as the aforementioned CoNi@NC-600 catalyst, and was named as Co@NC. The preparation process for the Ni@NC catalyst was identical to that of the Co@NC catalyst,

with the difference being that the precursor used was Ni-PBA. The characterization of the materials and details of the associated tests can be found in the supporting information.

Acknowledgements

The authors sincerely gratitude the support supplied by the Chongqing Technology Innovation and Application Development Project (No. CSTB2022TIAD-KPX0028) and the National Key Research and Development Program of China (No. 2023YFB3809500).

Conflict of Interests

The authors declare no conflict of interest.

Data Availability Statement

Research data are not shared.

Keywords: Prussian blue analogues • Bimetallic CoNi@NC • Oxygen reduction reaction • Mg-Air Batteries

- [1] X. J. S. Hou, K. Gaskell, P. Wang, L. Wang, J. Xu, R. Sun, O. Borodin, C. Wang, *Science* **2021**, *374*, 172–178.
- [2] S. Chu, A. Majumdar, *Nature* **2012**, *488*, 294–303.
- [3] L. Ellingsen, C. Hung, G. Majeau-Bettez, B. Singh, Z. Chen, M. Whittingham, A. Stremman, *Nat. Nanotechnol.* **2016**, *11*, 1039–1051.
- [4] Y. Chen, J. Xu, P. He, Y. Qiao, S. Guo, H. Yang, H. Zhou, *Sci. Bull.* **2022**, *67*, 2449–2486.
- [5] B. Lim, S. Lim, Y. Pang, S. Shuit, S. Kuan, *Renewable Sustainable Energy Rev.* **2023**, *184*, 113451.
- [6] T. Li, M. Huang, X. Bai, Y.-X. Wang, *Prog. Nat. Sci.* **2023**, *33*, 151–171.
- [7] T. Zhang, Z. Tao, J. Chen, *Mater. Horiz.* **2014**, *1*, 196–206.
- [8] J. Zhang, H. Zhang, Y. Zhang, X. Wang, H. Li, F. Feng, K. Wang, G. Zhang, S. Sun, Y. Zhang, *J. Mater. Chem. A* **2023**, *11*, 7924–7948.
- [9] L. Li, H. Chen, E. He, L. Wang, T. Ye, J. Lu, Y. Jiao, J. Wang, R. Gao, H. Peng, Y. Zhang, *Angew. Chem. Int. Ed.* **2021**, *60*, 15317–15322.
- [10] F. Tong, S. Wei, X. Chen, W. Gao, *J. Magnesium Alloys* **2021**, *9*, 1861–1883.
- [11] Y. Wang, Y. Sun, W. Ren, D. Zhang, Y. Yang, J. Yang, J. Wang, X. Zeng, Y. Nuli, *Energy Mater.* **2022**, *2*, 200024.
- [12] X. Chen, X. Liu, Q. Le, M. Zhang, M. Liu, A. Atrens, *J. Mater. Chem. A* **2021**, *9*, 12367–12399.
- [13] K. Leong, Y. Wang, W. Pan, S. Luo, X. Zhao, D. Leung, *J. Power Sources* **2021**, *506*, 230144.
- [14] F. Cheng, J. Chen, *Chem. Soc. Rev.* **2012**, *41*, 2172–2192.
- [15] Z. Huang, J. Wang, Y. Peng, C. Jung, A. Fisher, X. Wang, *Adv. Energy Mater.* **2017**, *7*, 1700544.
- [16] E. Timofeeva, C. Segre, G. Pour, M. Vazquez, B. Patawah, *Curr. Opin. Electrochem.* **2023**, *38*, 101246.
- [17] J. Milikić, A. Nastasić, M. Martins, C. Sequeira, B. Šljukić, *Batteries* **2023**, *9*, 394.
- [18] X. Lu, B. Xia, S. Zang, X. Lou, *Angew. Chem. Int. Ed. Engl.* **2020**, *59*, 4634–4650.
- [19] D. Liu, Y. Tong, X. Yan, J. Liang, S. X. Dou, *Batteries Supercaps* **2019**, *2*, 743–765.
- [20] C. X. Zhao, B. Q. Li, J. N. Liu, Q. Zhang, *Angew. Chem. Int. Ed.* **2020**, *60*, 4448–4463.
- [21] L. Yang, J. Shui, L. Du, Y. Shao, J. Liu, L. Dai, Z. Hu, *Adv. Mater.* **2019**, *31*, e1804799.
- [22] Z. He, L. Wang, M. Jiang, J. Xie, S. Liu, J. Ren, R. Sun, W. Lv, W. Guo, Y. Liu, B. Li, Q. Liu, H. He, *Rare Met.* **2024**, DOI: 10.1007/s12598-024-02767-w.
- [23] J. Liu, Z. Jin, X. Wang, J. Ge, C. Liu, W. Xing, *Sci. China Chem.* **2019**, *62*, 669–683.
- [24] Y. Leng, B. Yang, Y. Zhao, Z. Xiang, *J. Energy Chem.* **2022**, *73*, 549–555.
- [25] M. Li, M. Maisuradze, R. Sciacca, I. Hasa, M. Giorgetti, *Batteries Supercaps* **2023**, *6*, e202300340.
- [26] C. Xu, Z. Yang, X. Zhang, M. Xia, H. Yan, J. Li, H. Yu, L. Zhang, J. Shu, *Nano-Micro Lett.* **2021**, *13*, 166.
- [27] J. Yin, J. Zhou, Y. Wang, Y. Ma, X. Zhou, G. Wang, Y. Yang, P. Lu, J. Yu, Y. Chen, Y. Yuan, C. Ye, S. Xi, Z. Fan, *Small Methods* **2022**, *6*, 2201107.
- [28] S. Jung, P. Huong, M. Mapari, T. Thanh Tung, T. Kim, *Batteries Supercaps* **2024**, *7*, e202400091.
- [29] C. Deng, D. W. Wang, *Batteries Supercaps* **2019**, *2*, 290–310.
- [30] J. Chen, L. Wei, A. Mahmood, Z. Pei, Z. Zhou, X. Chen, Y. Chen, *Energy Storage Mater.* **2020**, *25*, 585–612.
- [31] X. Song, S. Song, D. Wang, H. Zhang, *Small Methods* **2021**, *5*, 2001000.
- [32] S. Ashraf, Y. Liu, H. Wei, R. Shen, H. Zhang, X. Wu, S. Mehdi, T. Liu, B. Li, *Small* **2023**, *19*, 2303031.
- [33] K. Zhao, Y. Shu, F. Li, G. Peng, *Green Energy Environ.* **2023**, *8*, 1043–1070.
- [34] D. Yu, Y. Ma, F. Hu, C. C. Lin, L. Li, H. Y. Chen, X. Han, S. Peng, *Adv. Energy Mater.* **2021**, *11*, 21012142.
- [35] M. Ahsan, A. Puente Santiago, Y. Hong, N. Zhang, M. Cano, E. Rodriguez-Castellon, L. Echegoyen, S. Sreenivasan, J. Noveron, *J. Am. Chem. Soc.* **2020**, *142*, 14688–14701.
- [36] X. Yu, Y. Feng, B. Guan, X. Lou, U. Paik, *Energy Environ. Sci.* **2016**, *9*, 1246–1250.
- [37] Q. Zhou, S. Miao, T. Xue, Y. Liu, H. Li, X. Yan, Z. Zou, B. Wang, Y. Lu, F. Han, *J. Colloid Interface Sci.* **2023**, *648*, 511–519.
- [38] Q. Xue, Y. Wang, M. Jiang, R. Cheng, K. Li, T. Zhao, C. Fu, *ACS Appl. Energy Mater.* **2023**, *6*, 1888–1896.
- [39] C. Tang, Q. Zhang, *Adv. Mater.* **2017**, *29*, 1604103.
- [40] K. Bhunia, E. Vijayakumar, N. P. Maria Joseph Raj, K. Serbara Bejigo, D. Kesavan, S. Kim, *Chem. Eng. J.* **2023**, *473*, 145028.
- [41] G. Hou, X. Jia, H. Kang, X. Qiao, Y. Liu, Y. Li, X. Wu, W. Qin, *Appl. Catal. B-Environ.* **2022**, *315*, 121551.
- [42] R. Li, X. Li, C. Liu, M. Ye, Q. Yang, Z. Liu, L. Xie, G. Yang, *Appl. Surf. Sci.* **2020**, *517*, 145841.
- [43] M. Zhang, Z. Wang, W. Li, A. Wang, Z. Song, Z. Huang, C. Hang, Z. Hu, *J. Alloys Compd.* **2023**, *952*, 170079.
- [44] Y. Wang, M. Chen, K. Zhang, H. Wu, J. Wang, Y. Cheng, Y. Liu, Z. Wei, *ACS Catal.* **2023**, *13*, 12601–12616.
- [45] Z. Li, H. Yang, H. Sun, S. Liang, G. Lu, Z. Liu, S. Kou, *A ACS Sustainable Chem. Eng.* **2021**, *9*, 4498–4508.
- [46] Q. Yang, Y. Jia, F. Wei, L. Zhuang, D. Yang, J. Liu, X. Wang, S. Lin, P. Yuan, X. Yao, *Angew. Chem. Int. Ed.* **2020**, *59*, 6122–6127.

Manuscript received: June 26, 2024
Revised manuscript received: July 18, 2024
Accepted manuscript online: July 22, 2024
Version of record online: September 6, 2024